JOURNAL OF GEOPHYSICAL RESEARCH: OCEANS, VOL. 118, 4184–4200, doi:10.1002/jgrc.20300, 2013

Summer nitrogenous nutrient transport and its fate in the Taiwan Strait: A coupled physical-biological modeling approach

Jia Wang,[1] Huasheng Hong,[1] Yuwu Jiang,[1] Fei Chai,[2] and Xiao-Hai Yan[1,3]

Received 25 March 2013; revised 10 June 2013; accepted 2 July 2013; published 5 September 2013.

[1] In order to understand the fate of nutrients in the Taiwan Strait during summer, we built a coupled physical-biological numerical ocean model, which can capture the basic hydrographic and biological features within the strait. The nutrient that we chose to model is dissolved inorganic nitrogen (DIN). The model includes individual reservoirs for nitrate (NO_3) and ammonium (NH_4). Both the observational evidence and model results show that NO_3 in the strait originates primarily from the upwelling subsurface water in the northern South China Sea (SCS) that enters the strait via the eastern and western routes separated by the Taiwan Bank. The coupled physical and biological effects on the NO_3 transport at these two routes are highlighted in the study. For the western route, the shallow topography and the coastal upwelling intensify the biological uptake of NO_3 in the whole water column. Consequently, the nitrogenous contribution by this route is mainly in form of the particulate organic nitrogen (PON). In contrast, NO_3 is transported conservatively below the nitricline at the deep eastern route, contributing the whole NO_3 supply in the TWS. The model estimates the fluxes of DIN and PON into the TWS, from the northern SCS, are 1.8 and 4 kmol s^{-1}, respectively. Over half ($\sim$1 kmol s^{-1}) of the DIN is synthesized into PON by the phytoplankton in the strait. Overall, this study estimates the physical and biological effects on the nutrient transport in the TWS during summer.

Citation: Wang, J., H. Hong, Y. Jiang, F. Chai, and X.-H. Yan (2013), Summer nitrogenous nutrient transport and its fate in the Taiwan Strait: A coupled physical-biological modeling approach, *J. Geophys. Res. Oceans*, *118*, 4184–4200, doi:10.1002/jgrc.20300.

1. Introduction

[2] The Taiwan Strait (TWS) is a shallow channel connecting South China Sea (SCS) and East China Sea (ECS) (Figure 1a). Under the effect of Asian monsoon, currents of the strait have an obvious seasonal variation [*Hu et al*., 2010]. The currents are complicated under the northeasterly monsoon in winter, e.g., the Chinese coastal current flows southward along the western coast of the TWS, while the extension of SCS warm current flows northward in main part of the TWS. The current is northward uniformly from SCS to ECS in summer, however recent studies show the SCS water intrudes into the strait via two routes (Figure 1b) at the southern TWS [*Jan et al*., 2010; *Hong et al*., 2011]. The western route is located between Taiwan Bank (TWB) and Guangdong coast; and the eastern route is stretch from the eastern TWB to Penghu Channel (PHC).

[3] In situ biogeochemical surveys show the upper layers of these two routes are characterized by oligotrophic SCS surface water, but the nutrient concentrations at the deep layers are high owing to the upwelling eutrophic SCS subsurface water [*Wu et al*., 2003; *Chen*, 2008; *Naik and Chen*, 2008]. The subsurface water can outcrops at the upwelling zones, leading to local high chlorophyll at the surface [*Hong et al*., 1991, 2009a; *Hu et al*., 2001; *Tang et al*., 2002, 2004; *Shang et al*., 2004]. Three main upwelling zones (Figure 1b), i.e., Dongshan Upwelling (DSU) off the Dongshan Island (DSI), Taiwan Bank Upwelling (TWBU) from the TWB to Penghu Island (PHI), and Pingtan Upwelling (PTU) off the Pingtan Island (PTI), exist at the strait almost all the summer. Except for the part upwelled to upper layers, the nutrient in the lower layers is transported downstream into the strait by the northward current. On its northward way, it is absorbed by the phytoplankton, leading to the nonconservative processes. However, the fate of the nutrients carried by these two sources has not been fully investigated so far.

[4] A coupled physical-biological numerical circulation model is an efficient tool to understand the nutrient fate associated with hydrodynamic and ecosystem processes [e.g., *Chen et al*., 1997; *Ianson and Allen*, 2002; *Dinniman et al*., 2003; *Chau*, 2005; *Fennel et al*., 2006; *Muttil and Chau*, 2006; *Druon et al*., 2010; *Gan et al*., 2010]. Different biological models have been applied in ecosystem simulations of the SCS and ECS [e.g., *Liu and Chai*, 2009;

[1]State Key Laboratory of Marine Environmental Science, Xiamen University, Xiamen, China.
[2]School of Marine Sciences, University of Maine, Orono, Maine, USA.
[3]College of Earth, Ocean and Environment, University of Delaware, Newark, Delaware, USA.

Corresponding author: Y. Jiang, State Key Laboratory of Marine Environmental Science, Xiamen University, Xiamen 361005, China. (ywjiang@xmu.edu.cn)

2169-9275/13/10.1002/jgrc.20300

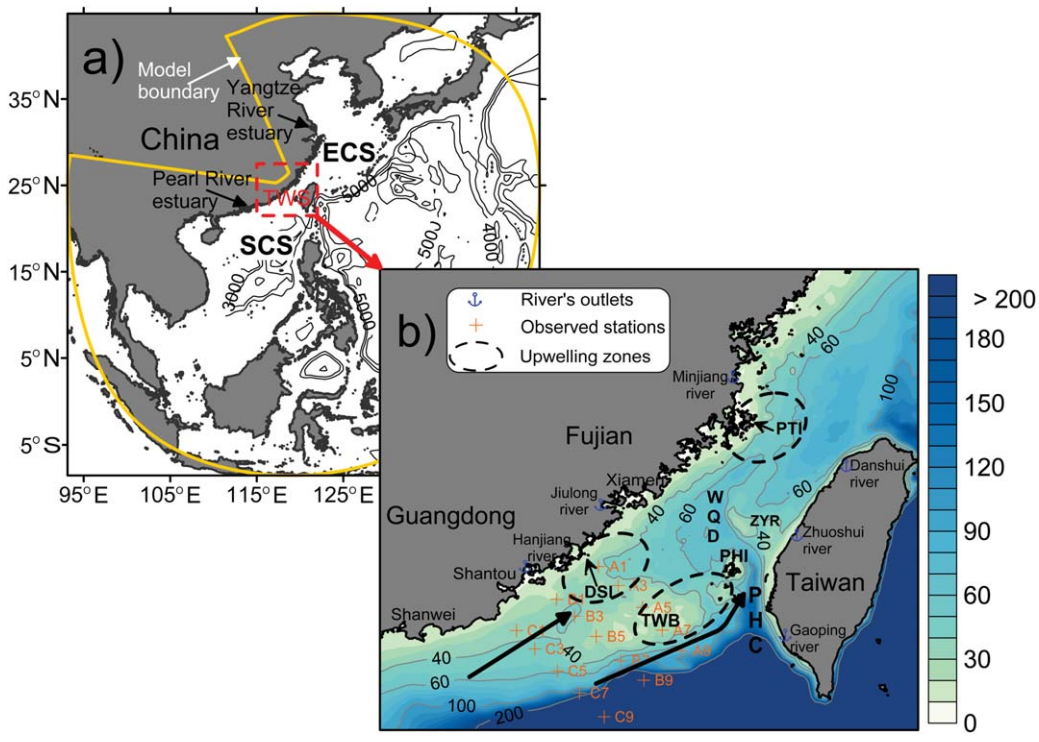

Figure 1. (a) Model domain and isobaths (units: m). (b) Bathymetry (with isobaths shown) of the Taiwan Strait and the adjacent sea, which is marked by the red dashed box in Figure 1a. The plus symbols indicate observed stations of sections A, B, and C, the blue anchor symbols indicate rivers' outlets, and the dash ellipses indicate upwelling zones. The two thick vectors indicate the western and eastern routes to the TWS. The abbreviations are listed in Table A1 of Appendix A.

Gan et al., 2010; *Liu et al*., 2010], but there are very few reports that focus on the TWS.

[5] The aim of this study is to track the nutrient fate, especially how the nutrient transport through the two routes during summer time in the TWS. The physical and biological model components are described in section 2, the model simulation results and the available biogeochemical observational data are summarized in section 3, and a set of sensitivity experiments are discussed in section 4. Section 5 discusses the nutrient supply, transport, and utilization within the TWS.

2. Numerical Model

2.1. Physical Model

[6] The numerical physical circulation model used in this study is the Regional Ocean Model System (ROMS) [*Shchepetkin and McWilliams*, 2005]. Under hydrostatic and Boussinesq assumptions, ROMS is a primitive equation model dealing with a curvilinear-orthogonal horizontal grid. An S-coordinate [*Song and Haidvogel*, 1994] was adopted in the vertical direction with finer resolution at surface and bottom, which is benefit to the simulation of the biological vertical structure in euphotic layer. In addition, the parallelization makes the model efficiency, particularly for the large grid number and longterm simulation.

[7] The modeling domain covers the northwestern Pacific from 93.13°E to 147.68°E and from 8.54°S to 44.9°N (Figure 1a) with spatial resolution that varies from 20 km at open boundary to 1 km in the TWS. The long semicircular curve across the north-eastern Pacific in Figure 1a is defined as open boundary with the other three boundaries being closed. The models bathymetry is interpolated from 2 arc-minutes global relief data collection (ETOPO2) combined with digitized depth data along the Chinese coast published by China's Maritime Safety Administration.

[8] The model was driven by climatological data on the open lateral and ocean surface boundaries. The initial and boundary conditions for temperature and salinity were derived from World Ocean Atlas 2005 (WOA-2005) (http://www.nodc.noaa.gov/OC5/WOA05/pr_woa05.html), and the imposed velocities at the lateral open boundary were derived from geostrophic currents computed from the WOA-2005 data. The surface forcing conditions are specified from the Atlas of Surface Marine Data 1994 [*Da Silva et al*., 1994]. Tidal forcing is imposed at the lateral boundary using the global database from Oregon State University TOPEX/Poseidon (T/P) Global Inverse model TPXO [*Egbert and Erofeeva*, 2002]. Freshwater inputs to the model are specified using monthly mean runoff data for the following rivers in the modeling domain: the Yangtze, Minjiang, Jiulongjiang, Hanjiang, Danshui, Zhuoshui, Gaoping, and Pearl River and were set as point sources at the appropriate points on the coastal boundary (Figure 1).

2.2. Biological Model

[9] The biological model coupled with the physical model is the modified nitrogen-based nutrient-phytoplankton-zooplankton-detritus (NPZD) model described by *Fennel et al*. [2006], the code of this NPZD model has been

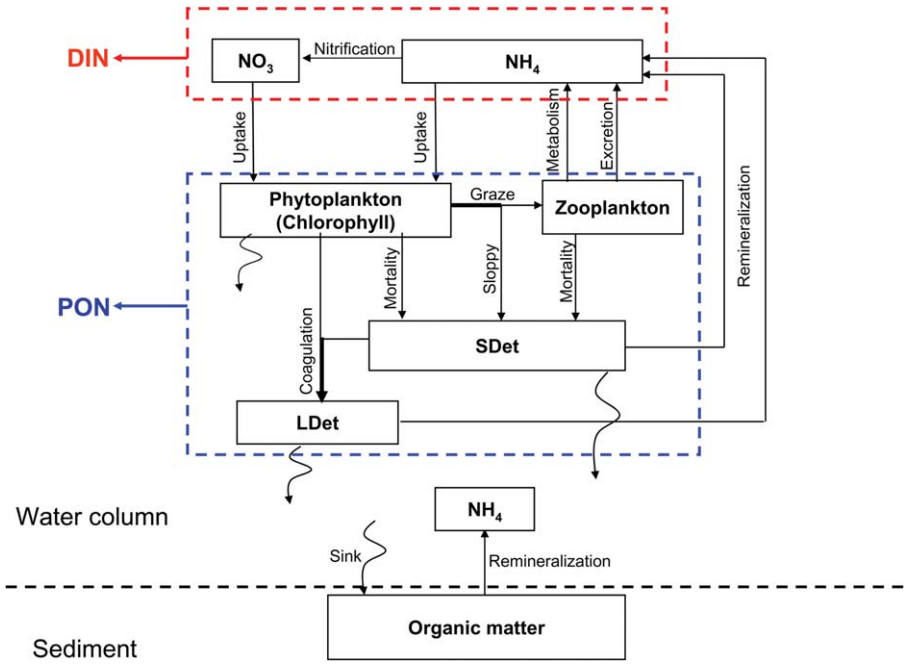

Figure 2. The Biological model schematic (SDet: Small detritus; LDet: Large detritus; DIN: Dissolved inorganic nitrogen; PON: Particulate organic nitrogen).

embedded in ROMS. The schematic model structure is shown in Figure 2. Like the structure of a classical NPZD model, the model includes seven state variables: nitrate (NO_3), ammonium (NH_4), phytoplankton, chlorophyll, zooplankton, Small Detritus (SDet), and Large Detritus (LDet). The nutrient pool is comprised of NO_3 and NH_4, which sustain the new productivity and regenerative productivity, respectively. Meanwhile the presence of NH_4 inhibits the NO_3 uptake by phytoplankton. The detritus is divided into SDet and LDet. The inefficient ingestion of phytoplankton and the mortality of phytoplankton and zooplankton are source terms for the pool of the SDet. The SDet can aggregate to form LDet together with the phytoplankton. A fraction of the detritus is mineralized into NH_4 in the water column with the remaining fraction sinking onto the seabed as the sediment.

[10] Because the most of biological formulas adopted by *Fennel et al*. [2006] are classic, such as the temperature dependent growth rate of phytoplankton [*Eppley*, 1972], photosynthesis-light (P-I) curve relationship [*Evans and Parslow*, 1985], and Holling-type grazing rate by zooplankton, and so on, therefore the biological parameters used in this study almost follows that in *Fennel et al*. [2006]. Nevertheless, a number of sensitivity experiments were carried out to evaluate these parameters, e.g., the growth rate of phytoplankton, maximal grazing rate by zooplankton, and so on, in the referenced range of 1 in *Fennel et al*. [2006, Table 1]. The results show that the adjustment of the parameters in a reasonable range did not change the pattern of the biological variable markedly.

[11] The structure of the model and equations are essentially the same as *Fennel et al*. [2006], except that we simplified the remineralization process for sediment. The benthic-pelagic coupling processes in the model was adopted from the formulae proposed by *Soetaert et al*. [2000] in which organic matter reaching the bottom is immediately remineralized back into the bottom water. While this parameterization of the remineralization is simplistic, *Soetaert et al*. [2000] showed through mass conservation, that it captures the essential dynamics of the benthic-pelagic coupling. The model result in this study also supports the rationality of this parameterization.

[12] The initial and boundary condition for NO_3 were derived from WOA-2005. The chlorophyll concentration was extrapolated in the vertical direction from surface values specified by the Sea-viewing Wide Field-of-view Sensor (SeaWiFS) monthly climatological data (http://oceancolor.gsfc.nasa.gov/) and the extrapolation is based on the generalized Gaussian curve of typical pigment profile [*Lewis et al*., 1983, *Morel and Berthon*, 1989]. The initial values of phytoplankton and zooplankton concentrations were set to 0.5 and 0.2 times the value of the chlorophyll concentration, respectively [*Liu et al*., 2002]. According to the measurement by *Xu et al*. [2005], NH_4 can be rapidly nitrified into NO_3 at the inner estuaries. Therefore, only NO_3 load from the rivers is considered in the model and the concentration is set to 25 μM according

Table 1. Skill Indices of MODIS and Model Compared With In Situ (SSC > 0.1 μg L^{-1})

	MODIS Versus In Situ		Model Versus In Situ	
Indices	SST	SSC	SST	SSC
Mb	0.91	−0.02	1.00	−0.56
R	0.87	0.66	0.86	0.70
RMS	1.79	0.53	2.10	0.74
RI	1.03	1.26	1.03	1.46

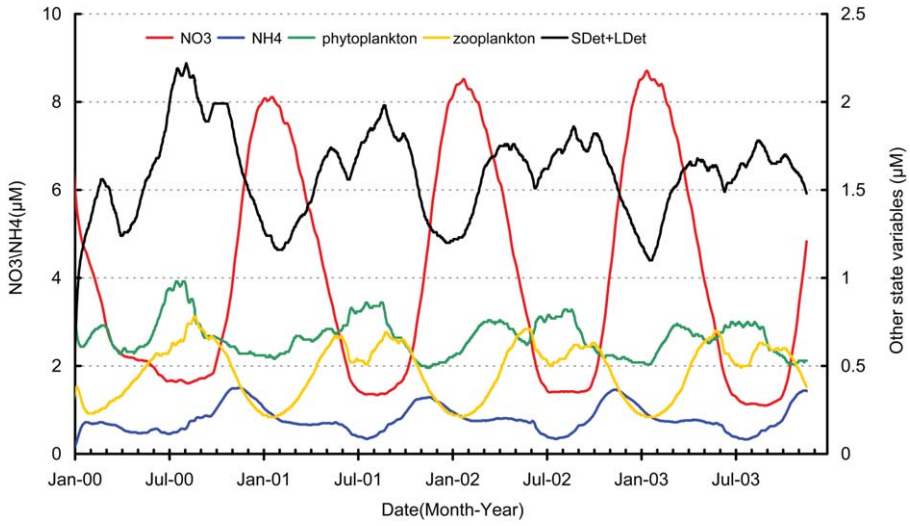

Figure 3. The time-serial variation of spatial mean concentration of the biological state variables during 4 year simulation.

to *Liu et al*. [2009] when there is not available in situ data. The organic nitrogen input from the rivers is not considered in the study. Photosynthetically available radiation at the sea surface was specified as the available fraction of the shortwave radiation intensity from Atlas of Surface Marine Data and the local latitude and longitude dependent diurnal variation of the shortwave radiation was included [*Niemela et al*., 2001].

[13] After the physical model had spun-up for 1 year since climatological 1 January, the coupled physical-biological has marched for four additional years and the results at the last year is analyzed in this study. The simulation is referred to as control run hereinafter. Figure 3 shows the time serials of spatial-average concentration of biological state variables in the TWS. Forced by the climatological data although, there is an unexpected interannual variation that is induced by the artificial initialization, model instability and system error maybe [*Liu et al*., 2002]. Nevertheless, compared with the seasonal variation, this interannual variation can be negligible after 2 year marching time. The NO_3 concentration reaches maximum in winter and lowest in summer, and the summer (July and August) and spring (March and April) blooms occur annually after second model year. The other variables are characterized by regular seasonal variation also, e.g., the variation of zooplankton lags that of phytoplankton by about 2 months, which reaches maximum twice a year too.

3. Model Results

[14] The model result is from the control run and some observational data in the TWS are available to validate the model. These include monthly climatological values for sea surface temperature (SST) and sea surface chlorophyll (SSC) with a spatial resolution of 4 km from the Moderate Resolution Imaging Spectroradiometer (MODIS) (http://oceandata.sci.gsfc.nasa.gov/MODISA/) and in situ hydrographic and biochemical data obtained from summer cruise in 2011. The cruise were designed to measure upwelling features in the southern TWS with sampling stations on three sections A, B, and C, which are marked at Figure 1b. Hydrographic measurements were taken with a SEB-917plus CTD abroad the *R/V Yanpin 2* and the biochemical samples were collected using SEB-hydrophore. Chlorophyll-a was measured using a standard fluorescence analysis and NO_3 was determined using standard spectrophotometric methods.

3.1. Current

[15] During the summer southwestern monsoon, the current (Figure 4) is northeastward along the Guangdong coast and bifurcates to the southwest of the TWB. Due to the surface and bottom Ekman effects, the currents trend offshore at the surface (Figure 4a) and onshore at the bottom (Figure 4b), which generates a compensatory onshore flow near the bottom of the eastern Guangdong shelf. This is in agreement with observations and other previous numerical studies [*Gan et al*., 2009; *Hu et al*., 2011], which suggested that the subsurface cold water off the Shanwei shelf break climbs onto shelf at the head of the widened continental shelf and advects northeastward along the Guangdong coast, ultimately outcropping in the lee of the cape near Shantou (Figures 4a). The bottom temperature distribution (Figure 4b) in the model also shows low temperature water (24–26°C) from the shelf-break offshore of Shanwei stretching into the near-shore region off DSI.

[16] At the eastern edge of the TWB, the northward current is strong in the upper layers. Both wind-driven upwelling and strong tidal mixing are proposed as mechanisms for bringing deep water onto the shelf in the northeastern TWB [*Jiang et al*., 2011]. Subsurface water in the northern SCS intrudes into the TWS via the PHC, which can lead to a strong onshore current [*Allen and Durrieu de Madron*, 2009]. Because of the shoaling across the Zhangyun Rise (ZYR), the northward near-surface current rotates clockwise in order to conserve potential vorticity [*Jan et al*., 1994], while the bottom flow is constrained by the topography to follow the sharp curve of the isobaths.

[17] It should be noted that low SST appears downstream of the PTI coast (Figure 4a) while there are onshore

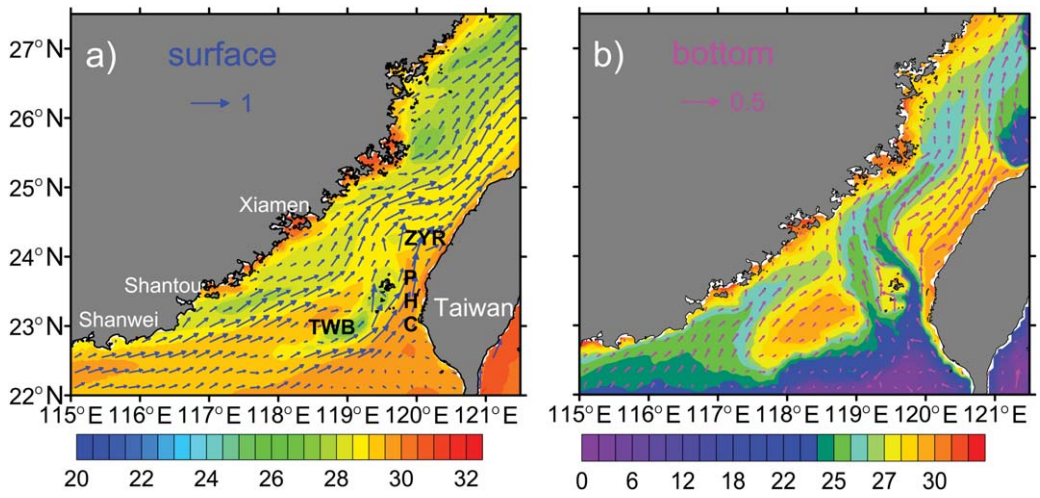

Figure 4. Modeled mean currents (m s^{-1}) in summer at (a) surface and (b) bottom, superimposed with surface and bottom temperature (°C) distributions, respectively.

currents between Xiamen and PTI coast in the bottom layer (Figure 4b). This phenomenon can be interpreted by the intensified upwelling processes in the lee of the cape related to the advection of vorticity [*Arthur*, 1965].

[18] Overall, the current pattern from the model agrees well with the previous studies of the region. Subsurface water rises up the slope of continental shelf in the northern SCS, and flows into the interior of the TWS via two routes [*Hong et al*., 2011], the route between the TWB and the Guangdong coast (hereafter the western route) and that through the PHC (hereafter the eastern route).

3.2. Model Verification

[19] To assess the model performance quantitatively, the skill indices, e.g., mean bias (Mb), correlation coefficient (R), root-mean-square (RMS) difference, and reliability index (RI) [*Stow et al*., 2009] are used (details in Appendix B).

3.2.1. SST and SSC

[20] A comparison of field data between model and MODIS are shown in Figure 5. Apparently, the model result resembles the MODIS image. SST at the southeastern TWS is higher than that at the northwestern TWS. Both the model result and MODIS image show that the SST is 1–2°C lower in the three main upwelling regions (PTU, DSU, and TWBU) than the surrounding water, which is consistent with the results reported by *Tang et al*. [2002]. In term of SSC, both MODIS and the model show that in the upwelling zones are higher than the surrounding water, also the model reproduces the oligotrophic SCS water occupying the southern and eastern TWS with lower chlorophyll (< 0.5 μg L^{-1}). The maximum chlorophyll concentration (> 5 μg L^{-1}) appears near the estuaries along the western coast of the TWS.

[21] Both the MODIS data and model result are verified with the in situ data (Table 1, the observing stations are plotted in Figure 1b). The SST comparison shows the model performance is similar with the MODIS. The index Mb indicates both the model and MODIS overestimate the SST by about 1°C. The RMS differences of SST are approximately 2°C for both model and MODIS. The MODIS and model SST have relative high correlations of $R = 0.87$ and $R = 0.86$, respectively, with the in situ SST. In term of RI, it closes to one for both MODIS and model, meaning high reliabilities of them.

[22] With regard to the SSC, Mb $= -0.56$ μg L^{-1} indicates the model underestimates the SSC in average, while the MODIS performs much better with Mb $= -0.02$ μg L^{-1}. The similar value of R means the model captures the distribution pattern of SSC as the MODIS does. In term of the index RI, the model value (1.46) is larger than the MODIS value (1.26), but it is within the range of 1.36–1.56, the RI between the MODIS and in situ estimated by *Zhang et al*. [2006]. It means model reliability is acceptable also.

[23] Above all, the model reproduces the SST almost as well as the MODIS, e.g., both of them have a reasonable correlation and reliability. The model and MODIS also have similar patterns of the SSC, and the correlation and reliability between the model SSC and observed SSC are accepted comparing with the MODIS's results.

3.2.2. NO_3 and Chlorophyll Vertical Distribution

[24] In situ NO_3 (Figure 6) and chlorophyll (Figure 7) distribution along sections A, B, and C (see Figure 1b) in summer were used to not only analyze the cross-shelf structure of the biological fields but also to evaluate the model's ability to reproduce them in the TWS.

[25] Both observed and simulated NO_3 distributions show the presence of relative high NO_3 (>1 μM) seaward of the shelf break. An analogous structure is present in the in situ temperature and salinity distributions reported by *Hu et al*. [2011], so that upwelled water at the eastern edge of the shelf within the TWB involves not only low temperature and high salinity but also high nutrients. The high NO_3 levels (>1 μM) also exist in the bottom water near the inshore edge of the cross-shelf sections, which is consistent with the path of subsurface water described in section 3.1, though the concentration at the section B is underestimated to some extent. Additionally, this high NO_3 concentration along the coast clearly decreases from the south to north.

[26] A definite deviation between the model and in situ data exists at station C3. The high NO_3 appears at the

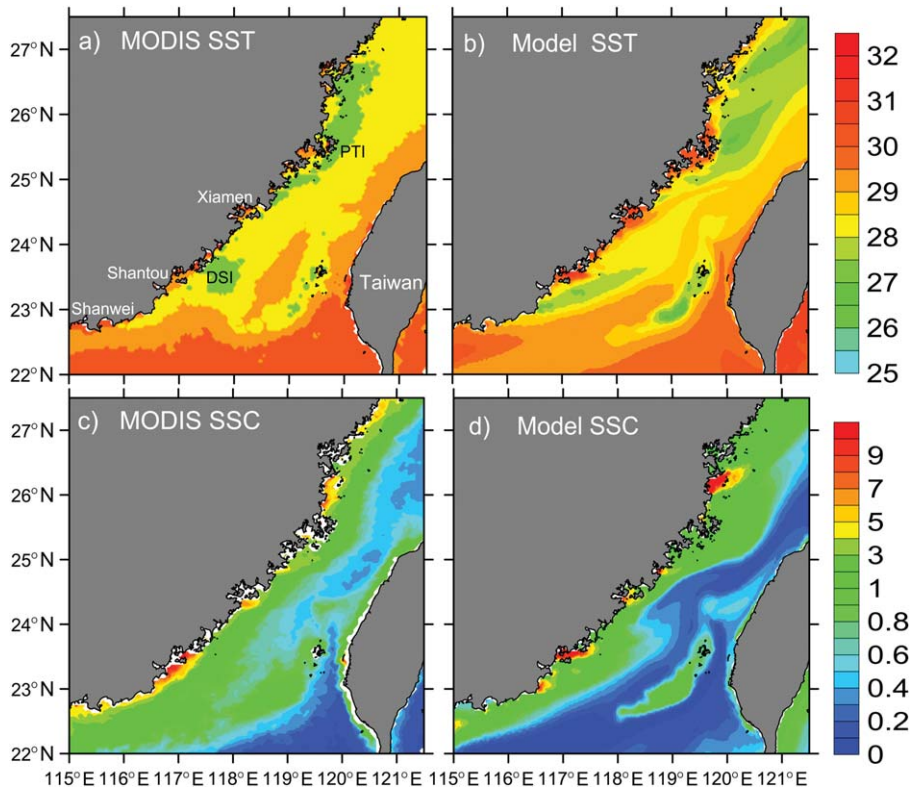

Figure 5. Comparison of modeled and satellite (MODIS) sea surface temperature (SST; °C) and sea surface chlorophyll (SSC; μg L^{-1}). The model fields are monthly mean result in July. The MODIS field is monthly mean field in July over the period from 2002 to 2012. (a) MODIS SST, (b) model SST, (c) MODIS SSC, and (d) model SSC.

surface of C3 in observation, but the model failed to reproduce it. According to the studies by *Hong et al*. [2009b] and *Hu et al*. [2011], the high NO_3 is source from the diluted water, which can be traced back to the Pearl River. From consideration of the simulated surface salinity distribution (not show), the model appears to adequately represent the dilution of the Guangdong coastal water with a low salinity tongue in the western TWB, but it underestimates the NO_3 concentration. The later analysis shows the NO_3 within the diluted water is completely depleted by photosynthesis before it is carried to the Shantou-DSI coast in the model.

[27] With respect to chlorophyll, the high concentrations exist along Guangdong-Fujian coast and in the subsurface waters above the shelf break of TWB in both the observations and the simulation results. In section A, the patterns of simulated and observed chlorophyll agree quite well, with high chlorophyll (>2 μg L^{-1}) existing at both station A1 and A7. In section C, both the model and observation capture the high chlorophyll concentration (>0.5 μg L^{-1}) in the subsurface centered around the depth of 40 m, which is known as the subsurface chlorophyll maximum (SCM) in the continental shelf of northeastern SCS [*Lu et al*., 2010]. In section B, the model overestimates the chlorophyll concentration in station B1, the resemblance between the model and observation is fair, but the characters of near-shore high chlorophyll and SCM at shelf break are reproduced by the model.

[28] Quantitative comparison of indices is shown in Table 2. The high correlation ($R = 0.89$) indicates the model captures the vertical structure of the NO_3 at the sections well. The mean bias of NO_3 between the model and observation is acceptable (Mb = 0.13 μM). However, the RMS (0.6 μM) and the reliability (RI = 1.35) of the model is relative large, which may be caused by the overestimated NO_3 at the lower layers of eastern shelf break of TWB in the model.

[29] By contrast, the model performance ($R = 0.59$ and RMS = 0.95 μg L^{-1}) of the chlorophyll distribution is not as satisfied as the results at surface in Table 1 ($R = 0.70$ and RMS = 0.74 μg L^{-1}). The reason is the improper resemblance of chlorophyll between the model and observation in section B. When the data along section B is removed from the verification, R significantly increases to 0.93 and the RMS decreases to 0.41 μg L^{-1} (Table 2). The reliability of the model also enhances to a high level (RI = 1.19).

[30] In general, the simulated NO_3 and chlorophyll resembles the main structure of the observation data. For examples, high NO_3 at bottom layer near shore and around shelf edge, chlorophyll concentrated at the subsurface around the shelf edge and through the whole water column near the shore. Above all, both the pattern and quantitative verification show the model reproduce the observation data reasonably.

4. Sensitivity Experiments

[31] As described in section 3.2.2, the model overestimates the chlorophyll concentration at the inner shelf off Guangdong-Fujian coast, while underestimates the NO_3

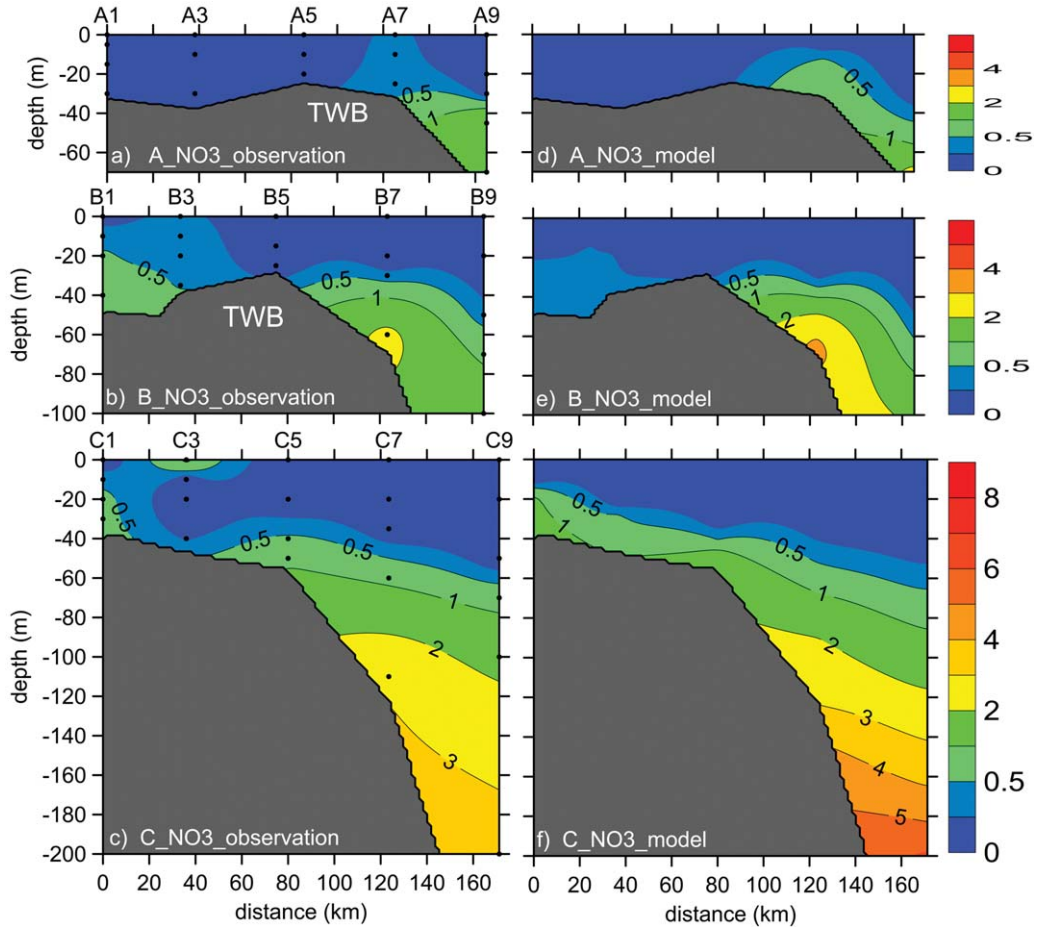

Figure 6. Summer NO_3 (μM) distribution along sections A, B, and C from the observation in (left) 2011 and (right) model. The observation stations in sections are marked with black dots.

concentration. The reason may be deduced by the overestimated growth rate of phytoplankton in the model. Therefore, the sensitivity experiments listed in Table 3, in order to limit the phytoplankton growth, are carried out to evaluate the model response to the parameter adjustment.

[32] The photosynthesis available light is attenuated by not only the chlorophyll (in Control run; Cases 2 and 3) but also the detritus (in Case 1) in the model [*Neumann*, 2000]. In Case 2, the attenuation coefficient of short radiation by chlorophyll is increased from 0.025 to 0.04 $mg^{-1} m^{-2}$. In Case 3, the base of temperature dependent growth function of phytoplankton [*Eppley*, 1972] is reduced from 1.066 to 1.055 according to *Macías et al*. [2012], who mention that this function affects phytoplankton growth rate in the Southern California upwelling ecosystem.

[33] The experiment results can be illustrated by the NO_3 (Figure 8) and chlorophyll (Figure 9) distributions along sections A, B, and C. As expected, limitations of the uptake by phytoplankton obviously lead to higher NO_3 concentration at the inner shelf of section B in three cases, especially in Cases 1 and 2 than that in control run (Figure 6). In Case 2, the increasing NO_3 occurs at not only the inner shelf but also the shelf break (right part pf the sections). For the same reason, the chlorophyll concentrations along the three sections decrease to some extent, especially at TWBU in Cases 1 and 2. It is also noticeable that in Cases 1 and 2, chlorophyll concentrations at lower layers decrease while at surface increase due to the higher attenuation of light. By contrast, the adjustment in Case 3 modifies the chlorophyll and NO_3 distributions less.

[34] To evaluate the model performances in these sensitive experiments, the Taylor diagram (Figure 10) [*Taylor*, 2001; *Stow et al*., 2009] is used to compare the simulated NO_3 and chlorophyll with observation in sections A, B, and C. The diagram provides a concise statistical summary of the *R*, standard deviation (σ), and the centered RMS difference (E′, Appendix B). Because the units of NO_3 and chlorophyll are different, the centered RMS difference and the standard deviations are normalized by the standard deviation of the corresponding observations [*Taylor*, 2001]. Table 4 lists the bias between the model and observation, as Taylor diagram filters out the bias information.

[35] In Case 1, considering the detritus shading effect of light, the R and E′ of chlorophyll are obviously improved, while those of NO_3 become worse (Figure 10) although the NO_3 concentration increases at the inner shelf of section B (Figure 8) as we expected. The Mb in Table 4 shows the same changing pattern, i.e., the chlorophyll's bias decreases while the NO_3's bias increases. In Cases 2 and 3, both the NO_3 and chlorophyll have higher mean bias than the control run, the R and E′ of NO_3 become significantly worse in Case 3.

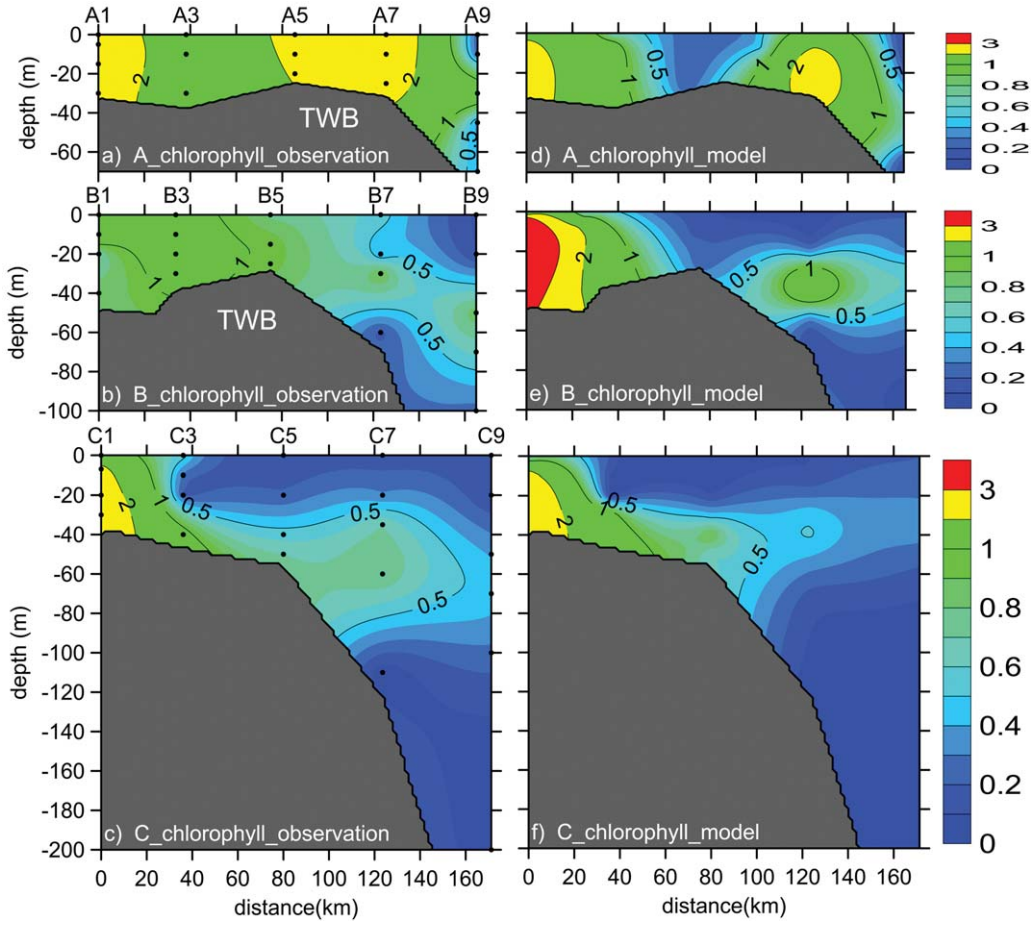

Figure 7. Summer chlorophyll (μg L^{-1}) distribution along sections A, B, and C from the observation in (left) 2011 and (right) model. The observation stations in sections are marked with black dots.

[36] Above all, the modeling performance cannot be improved generally as we expect in the sensitivity tests, as every parameter adjustment may modify the whole biological system simultaneously, e.g., the attenuation of short radiation can reduce the chlorophyll at both the inner and outer shelf, while increasing/decreasing it at upper/lower layer. Therefore, the experiment results indicate parameter shall be elaborated systematically, and more processes (e.g., suspended sediment processes) shall be considered to achieve better biological modeling performance, while the physical model shall reproduce the correct hydrodynamic processes basically.

5. Discussion

[37] Although the nutrient concentration is relatively low at surface of the TWS in summer, both the model results and observation show the enrichment of NO_3 that occurs near the shelf break of TWB and near the bottom in the near-shore region along the Guangdong-Fujian coast, introduced by the upwelling SCS subsurface water [*Gan et al.*, 2009; *Hu et al.*, 2011]. The hydrographic analysis in section 3 indicated that the subsurface water intrudes into the TWS via two routes. Using numerical modeling, we diagnosed the NO_3 transport and the physical-biological effects on it as it moves along the two routes. We also analyzed the relative contributions from the two routes on the nitrogenous flux through the TWS.

Table 2. Skill Indices of Model Compared With In Situ Profiles in Sections ($NO_3 > 0.05$ μM and Chlorophyll > 0.1 μg L^{-1})

Indices	Sections	Mb	R	RMS	RI
NO_3	A, B, C	0.13	0.89	0.60	1.35
Chlorophyll	A, B, C	0.08	0.59	0.95	1.35
Chlorophyll	A, C	−0.18	0.93	0.41	1.19

5.1. Nutrient Transport Along the Two Routes

[38] The distribution of NO_3 near the bottom in Figure 11a shows that high NO_3 concentrations stretch from the

Table 3. Sensitivity Experiments on Limitation of Phytoplankton Growth

Experiment	Description
Control	Control run as described in section 2
Case 1	Add attenuation of short radiation by SDet and LDet with the coefficient 0.01 $(\mu M)^{-1}$ m^{-1}
Case 2	Increase attenuation coefficient of short radiation by chlorophyll from 0.025 to 0.04 mg^{-1} m^{-2}
Case 3	Decrease base of temperature dependent growth function of phytoplankton from 1.066 to 1.055

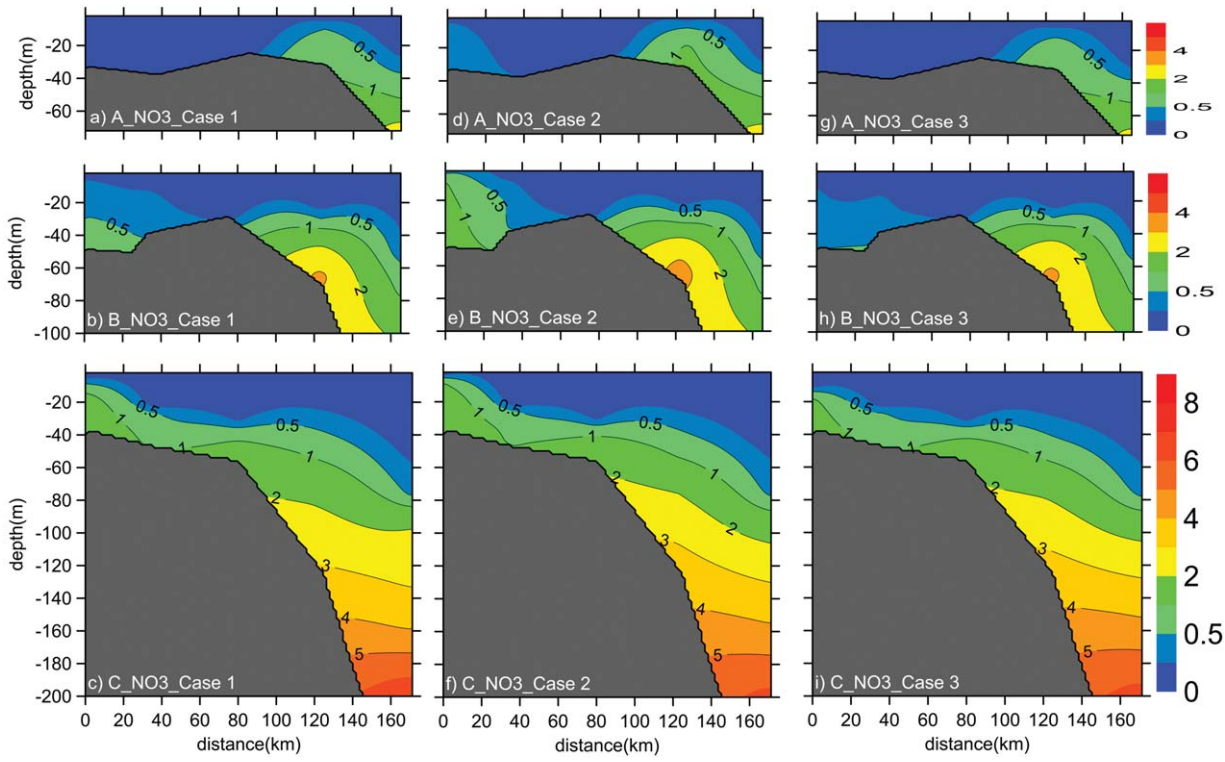

Figure 8. NO_3 (μM) distributions along sections A, B, and C of sensitivity experiments (Cases 1–3).

northern SCS to the inner TWS via the western and eastern routes, which are consistent with the intrusion of the subsurface SCS water described in section 3.1. By contrast, NH_4 concentrations are lower in the deep sea, but are higher ($\sim$3 μM) at both the Guangdong coast and the eastern edge of the TWB (Figure 11b), which is related to the regenerative production processes.

[39] The observed high NO_3 in the inner shelf (Figure 6) is attributed to nutrient transport from the western route, while inputs from the eastern route can explain the observed high NO_3 off the Xiamen coast during June to July 2009 (Figures 11c and 11e). The simulated NO_3 distributions (Figures 11d and 11f) along sections X3 and X5, characterized by high NO_3 concentration ($>$1 μM) located

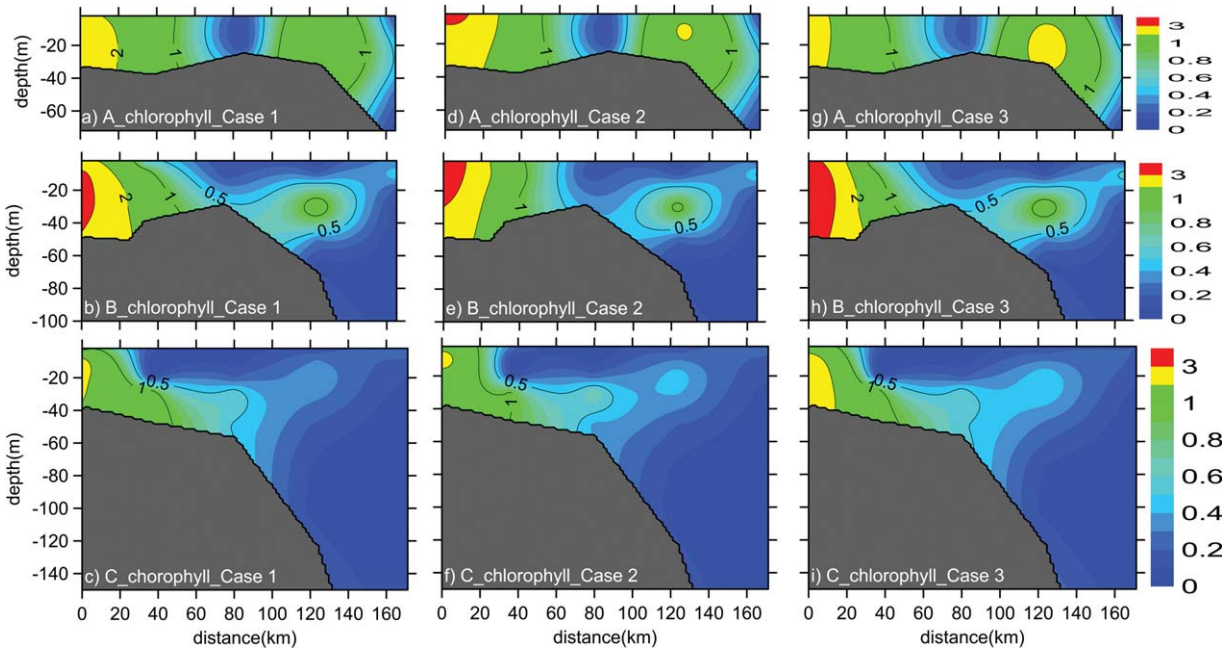

Figure 9. Chlorophyll (μg L^{-1}) distributions along sections A, B, and C of sensitivity experiments (Cases 1–3).

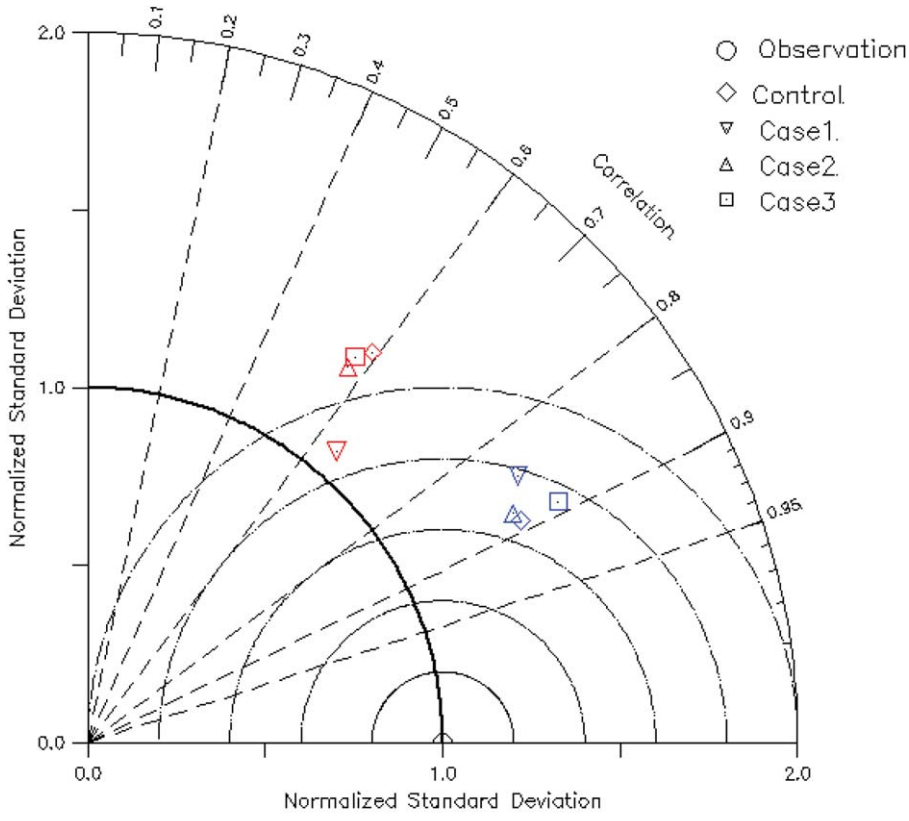

Figure 10. Taylor diagram for differences between modeled NO_3 (blue symbols) and chlorophyll (red symbols) with observation (black circle at coordinate (1, 0)) in sections A, B, and C. The radial distance from the origin is proportional to the ratio standard deviations; the distance between the model points and the observed point indicates the centered RMS difference; the azimuthal positions indicate the correlation coefficient. The centered RMS and standard deviations are normalized by standard deviation of observation.

at the Wuqiu Depression (WQD; northern extension of the PHC), are consistent with the observations. The extensive flooding of the Jiulongjiang River during the cruise caused higher than normal NO_3 at the surface 40 km offshore in section X3 (Figure 11c), which cannot be represented by a model driven with climatological forcing.

[40] As the cool and eutrophic subsurface water intrudes into the TWS from the south, it loses its original characters gradually when mixed with surrounding warm and oligotrophic water (Figures 4b and 11a). The temperature and NO_3 distributions along the two routes are sampled at two sections in Figure 11 (the sections are labeled with WR and ER in Figure 11a). It shows the warm ($> 28°C$) and oligotrophic SCS surface water is limited in the surface, while the cool ($<27°C$) and eutrophic ($> 0.80\ \mu M$) SCS subsurface water dominates the lower layer, forming thermocline between them, as well as the nitricline. Considering the transportation below the thermocline, the horizontal distance between 25 and 26°C isotherm is about 120 km at the section WR (Figure 12a), while at the section ER it is about 150 km (Figure 12b). Within the corresponding distance of 25 and 26°C isotherm, the NO_3 decreases from 1.50 to 0.25 μM at the section WR (Figure 12c) and from 1.40 to 0.80 μM at the section ER (Figure 12d). Obviously, NO_3 decreases faster at the western route than the eastern route.

[41] Since the NO_3 transport at the routes are determined by not only mixing process but also biological effect, the bottom temperature and NO_3 variations of the two sections are plotted in Figure 13 (within the subsection between 25 and 26°C isotherm). The parallel curves of temperature indicate the mixing intensities are similar between the two sections, except for that at 180–220 km of the section ER where the topography is sunk and the temperature keeps almost constant. By contrast, the decreasing rate of NO_3 at the section WR is about twice as large as that at the section ER, which is attributed to the greater biological depletion of NO_3 in the section WR.

5.2. The Physical-Biological Effects on the Nutrient Transport

[42] In order to clearly understand the physical and biological effects on the nutrient transport in the TWS, we

Table 4. Mean Bias Between Sensitivity Experiments and Observation in Sections A, B, and C.

	Control	Case 1	Case 2	Case 3
NO_3 (μM)	0.13	0.32	0.43	0.22
Chlorophyll ($\mu g\ L^{-1}$)	0.08	−0.02	0.09	0.09

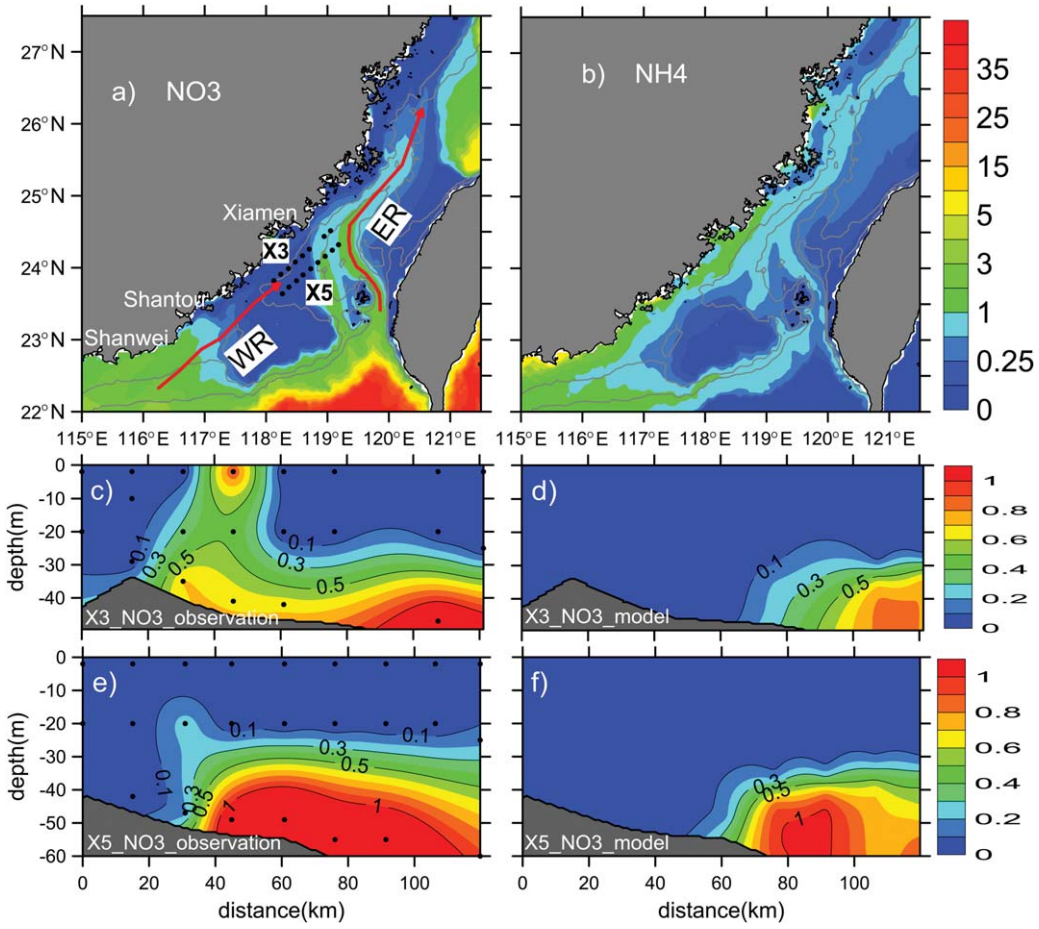

Figure 11. Distributions of (a) NO_3 and (b) NH_4 at bottom from model (units: μM). NO_3 distributions in June 2009 (c and d) along section X3 and (e and f) section X5 from the observation (left) and model (right). The observation stations in sections X3 and X5 are marked with black dots in Figure 11a. The sampling section WR and ER at the western and eastern routes, respectively, are marked with red arrowed lines in Figure 11a.

diagnosed each term of the tracer equation for NO_3 along section WR (Figure 14) and section ER (Figure 15). The right-hand side includes advection, diffusion, biological uptake, and nitrification terms. The first two terms are physical terms, while the latter two are biological terms.

$$\partial[\mathrm{NO_3}]/\partial t = \underbrace{(-\vec{v}\cdot\nabla[\mathrm{NO_3}])}_{\text{advection}} + \underbrace{(k_T\nabla^2[\mathrm{NO_3}])}_{\text{diffusion}} + \underbrace{(-L_{NO3}\cdot[PHYTO])}_{\text{uptake}} + \underbrace{L_{nitri}\cdot[\mathrm{NH_4}]}_{\text{nitrification}} \quad (1)$$

physical term; biological term

where $\vec{v}$ is the three-dimensional velocity, k_T is the diffusion coefficient, L_{NO3} is the uptake rate of NO_3, [*PHYTO*] is the concentration of phytoplankton, and L_{nitri} is the nitrification rate.

[43] At a steady state, i.e., the left-hand side of the equation equals to zero, the positive physical terms (Figures 14c and 15c) and the negative biological (Figures 14f and 15f) terms are counterbalanced by each other. It means the physical effect sustains the biological depletion of NO_3 in the strait.

[44] In term of the physical effect, the positive values of advection term (Figures 14a and 15a) mean the high NO_3 within the SCS subsurface water is transported downstream below the nitricline; the positive values in diffusion term (Figures 14b and 15b) mean the NO_3 below the nitricline is transported upward to the nitricline by mixing effect. Consequently, the advection and diffusion effects supply the NO_3 below and in the nitricline, respectively. Above the nitricline, neither advection nor diffusion process carries NO_3 due to the oligotrophic SCS surface water and the stratification in the nitricline blocking of the nutrient replenishment from deep layers.

[45] In addition to that, the upwelling effect, marked with the light blue box in Figures 14a and 15a, is noticeable by the intensification of the vertical advection of NO_3 to the surface at the DSU (100–200 km in the section WR) and the PTU (250–300 km in the section ER), respectively, which correspond to the maximum uptake rate there.

[46] With regard to the biological effect, the nitrification on the source of NO_3 (Figures 14d and 15d) can be neglected because the rate is two orders of magnitude smaller than the uptake rate (Figures 14e and 15e). The uptake varies vertical depending upon the light intensity and NO_3 supply. Below the nitricline, NO_3 is plentiful from the advective contribution but the uptake of it is

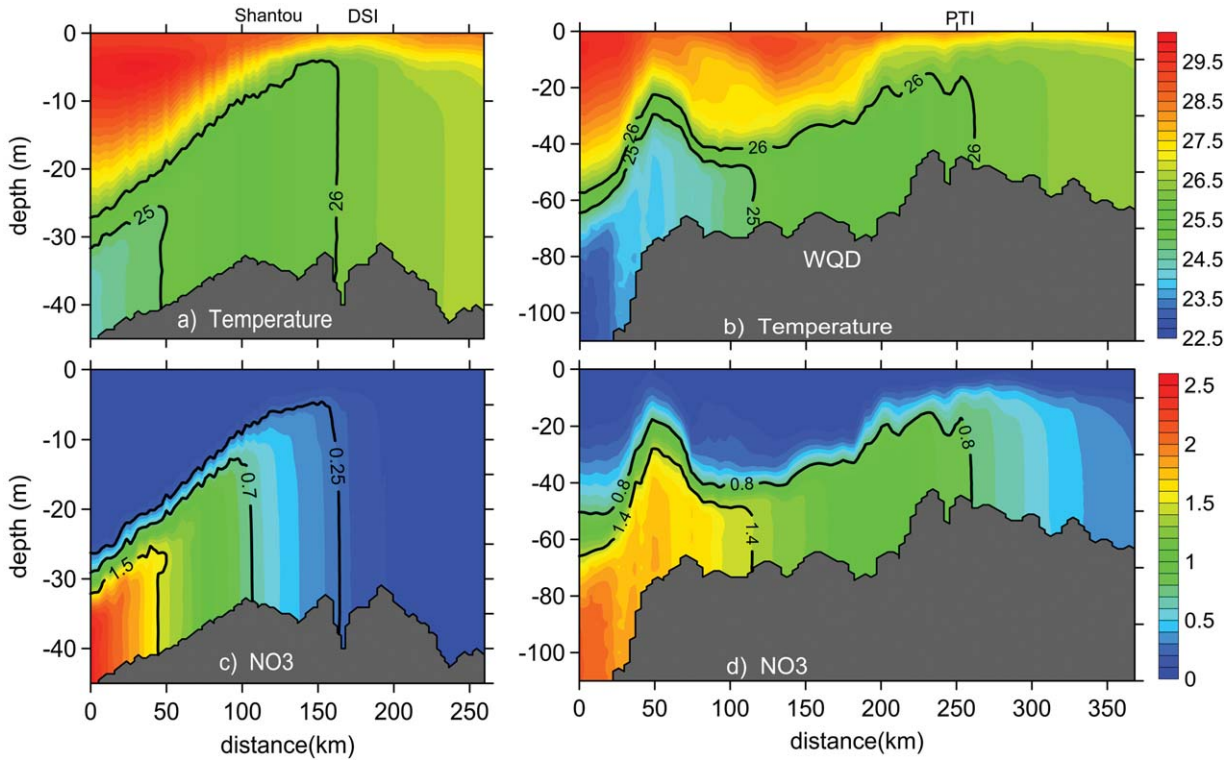

Figure 12. Distributions of temperature (°C) and NO_3 (μM) along the sections (left) WR and (right) ER in the model.

limited by inadequate light levels. Above the nitricline, light is sufficient for the photosynthesis but the insufficient NO_3 supply limits the uptake rate of it except in the upwelling zones (as shown in Figures 14e and 15e) where the physical effect can supply enough NO_3 to the surface. The upwardly transported NO_3 exposing to the intense light is almost depleted by the photosynthesis, so the nutrient levels are low at the surface. In the nitricline, there is not only an adequate supply of NO_3 replenished from deeper layers by diffusive effect but also sufficient light for the photosynthesis, thus the NO_3 uptake reaches its maximum in vertical water column.

[47] The influences of the biological effect are significantly different at the two routes. In the western route where the depth is less than 40 m, the light can penetrate through the water column, and the euphotic layer is deeper than the nitricline. As a result, there are correspondingly large biological uptake rates (0.05–0.25 μM day^{-1}) below the nitricline, most of which are located in the depth with $NO_3 > 0.7$ μM (Figure 14e). Namely, the high-concentration NO_3 at the lower layer of the western route can be considerably depleted by phytoplankton. In addition to that, the coastal upwelling carries the NO_3 to the upper layers at the distance between 100 and 200 km (Figure 14a), which further enhances the biological uptake of NO_3 (Figure 14e). Therefore, the transport distance of the NO_3 at the western route can be greatly shorted by the biological uptake.

[48] Compared with the western route, the nitricline is deeper at the eastern route (Figure 15d). The NO_3 consumption at the eastern route is restricted in the nitricline mainly (except for the PTU area around 250–300 km) due to the insufficient nutrient and light above and below the nitricline, respectively. Thus, the biological uptake rate is low (<0.05 μM day^{-1}) below the nitricline, as shown by the red shade in Figure 15e, indicating the high-concentration (>0.8 μM) NO_3 in this route is less influenced by biological effect. Therefore, the fate of NO_3 below the nitricline approaches a conservative process before it reaches into PTU area at the eastern route, which contributes the long transport and the main supply of NO_3 in the TWS.

[49] In general, the advection and diffusion effects supply the NO_3 under and in the nitricline, respectively. The biological depletion of NO_3 assembles around the nitrciline owning to both the physical transportation and light

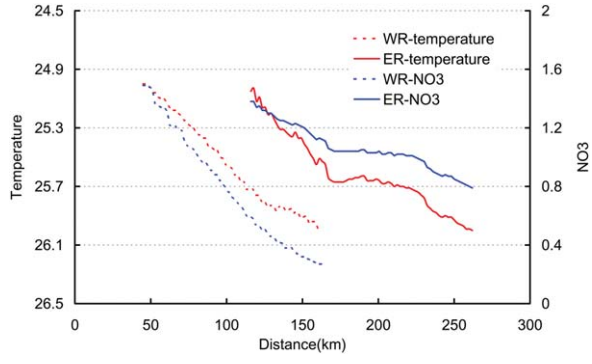

Figure 13. The variations of bottom temperature (°C) and NO_3 (μM) at sections WR and ER.

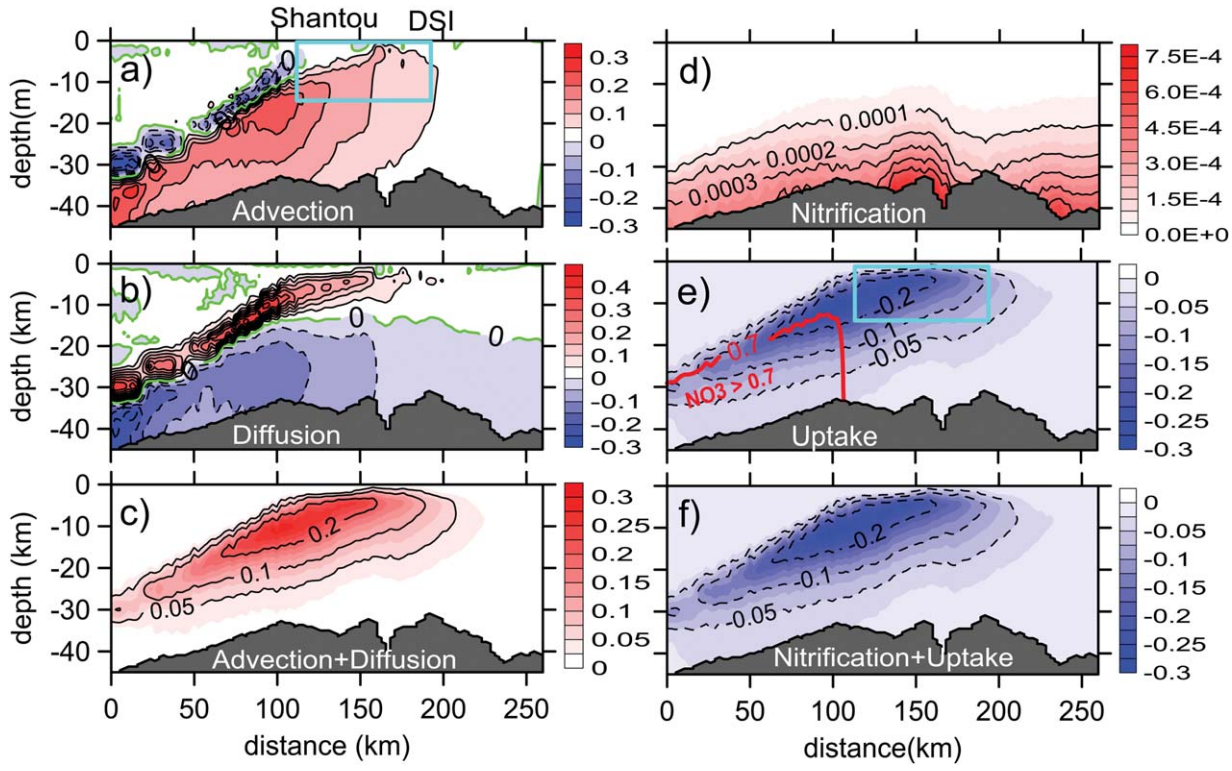

Figure 14. Diagnostic terms (include (a) advection, (b) diffusion, (d) nitrification, and (e) uptake) in the NO_3 equation along section WR (units: μM day^{-1}). The boxes in Figures 14a and 14e indicate upwelling region and the red isoline in Figure 14e presents the concentration of $NO_3 = 0.7$ μM. (c) The physical term includes advection and diffusion terms. (f) The biological term includes nitrification and uptake terms.

condition. The shallow topography and upwelling enhance the biological depletion of NO_3 in the whole water column at the western route, which greatly shortens the transport distance of NO_3. By contrast, the topography is deep at the eastern route and the NO_3 transportation is conservative below the nitricline.

5.3. Contributions of the Two Nutrient Routes

[50] Since the biological effect is significant at the western route, the nutrient contribution from the route is greatly influenced by it. Sections S1 and S2 were placed in the southern TWS (Figure 16a) to compute the relative contributions from the western and eastern routes. In this study, nitrogen is classified into DIN and PON as shown in Figure 2. The former (DIN) includes NO_3 and NH_4, while the latter (PON) includes phytoplankton, zooplankton, SDet, and LDet. The sum of the DIN and PON is defined as the total nitrogen (TN).

[51] The NO_3 flux through section S2 is 25 times larger than that through S1 as shown in Figure 16b, which meaning that the eastern route contributes nearly all of the NO_3 in the TWS. However, the PON input cannot be neglected because it can be remineralized into NH_4 and contribute to the regenerative productivity in the strait. In terms of TN fractionation, both routes present a higher flux of PON than DIN (Figure 16b). Especially for the western route, it contributes approximately 45% of the PON to the TWS even though it comprises only 25% of the water volume and 10% of the DIN.

[52] Employing the definition of the Degree of Nutrient Consumption [DNC = DON/(DON + DIN)] by *Chen et al*. [2004], the DON is the dissolved organic nitrogen and the PON in this model is labile as DON, the mean DNC over sections S1 and S2 are 0.91 and 0.58, respectively. These agree well with the DNC distribution in the southern section observed by *Chen et al*. [2004], which found DNC exceeding 0.9 in the western section and roughly 0.6 in the eastern section. Both the model results and observation indicate a rapid biological consumption of upwelled nutrients in the two routes, especially in the western route where NO_3 is almost entirely exhausted.

[53] Besides the local biological utilization, the Pearl River's input also has an influence on the flux of TN in the western route. Although the model underestimates the NO_3 concentration in the diluted Guangdong coastal water, the numerical experiment without NO_3 input from the Pearl River, shows approximately 30% of the PON in the western route is contributed by the diluted water of Pearl River (Figure 16b).

[54] In general, the eastern route contributes nearly all of the NO_3 input into the TWS, primarily as DIN, while the western route contributes approximately 45% of the PON to the strait, of which about 30% is introduced by the Pearl River.

5.4. Nitrogenous Flux Through the TWS

[55] The DIN, which comes from the northern SCS, passes through the TWS and is transported into the ECS. During its transit, it is absorbed and transformed into PON by phytoplankton. Figure 17 shows the summer-mean fluxes of DIN and PON through a serial of sections, which are set from the south (sections S1 and S2) to the north

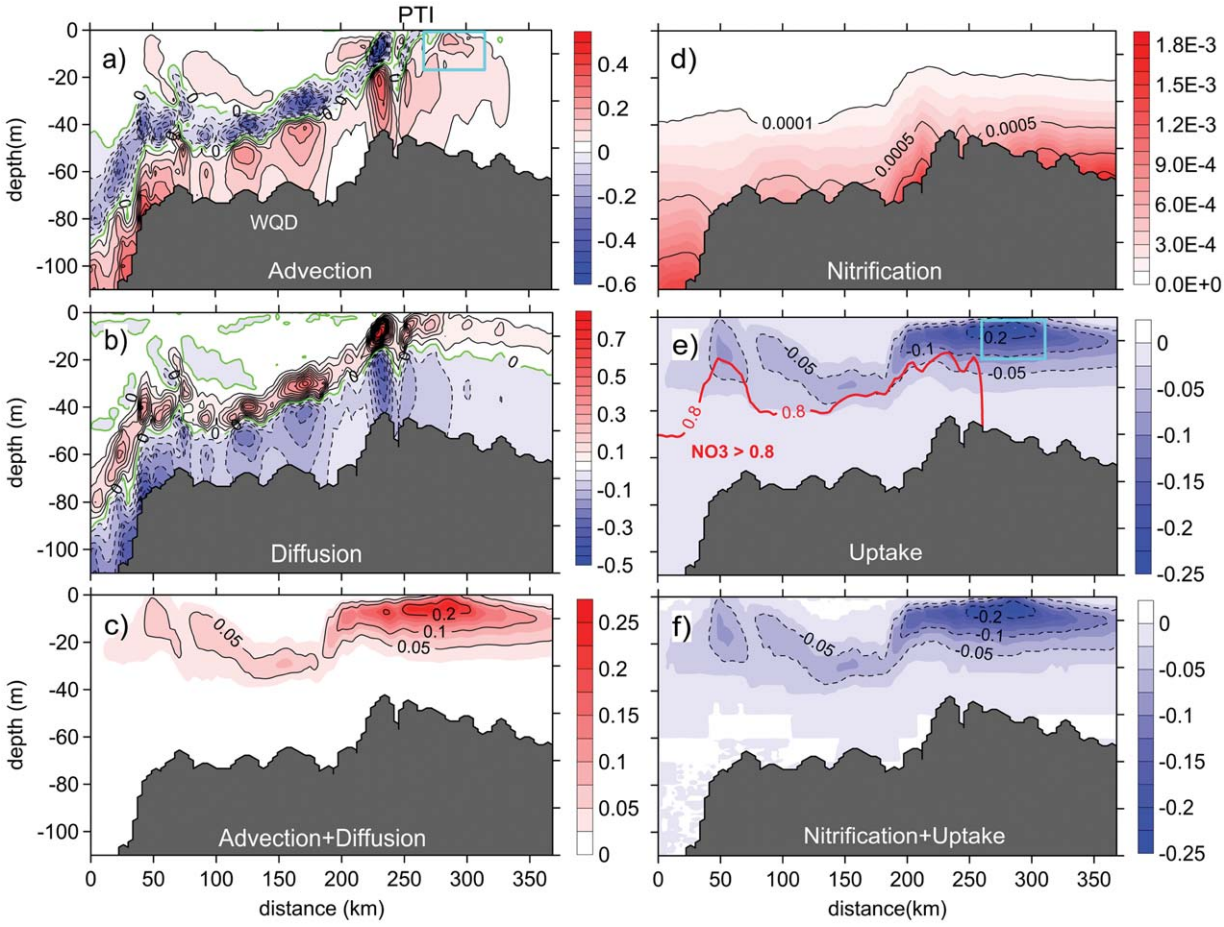

Figure 15. Diagnostic terms (include (a) advection, (b) diffusion, (d) nitrification, and (e) uptake) in the NO_3 equation along section ER (units: μM day^{-1}). The boxes in Figures 15a and 15e indicate upwelling and the red isoline in Figure 15e presents the concentration of $NO_3 = 0.8$ μM. (c) The physical term includes advection and diffusion terms. (f) The biological term includes nitrification and uptake terms.

(section S3) of the strait in Figure 16a. Compared with the DIN flux estimated by *Chung et al*. [2001] (1.8 kmol s^{-1} at about 220 km, marked with a red line in Figure 16a), the flux through the section is underestimated by the model. The difference is related with the model's inability to resolve the daily and interannual variation of the flux.

[56] Focusing on the nutrient fate in the TWS, Figure 17 shows that the DIN and PON input from northern SCS is

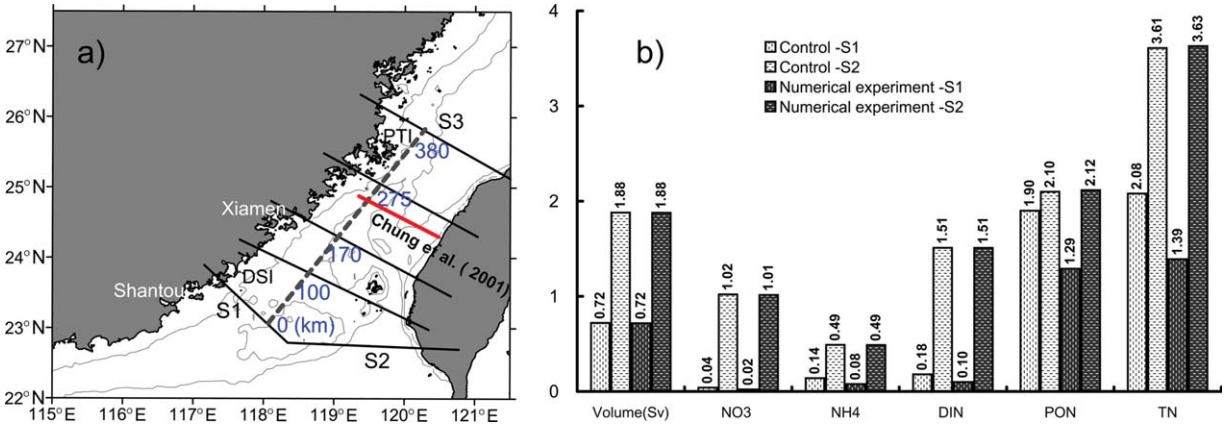

Figure 16. (a) Location of sections at the TWS. (b) Volume and nitrogenous fluxes (Units: Sv and kmol s^{-1}) of sections S1 and S2 in the control run and numerical experiment without NO_3 load from the Pearl River. (1 Sv = 10^6 m^3 s^{-1}; 1 kmol s^{-1} = 10^3 mol s^{-1})

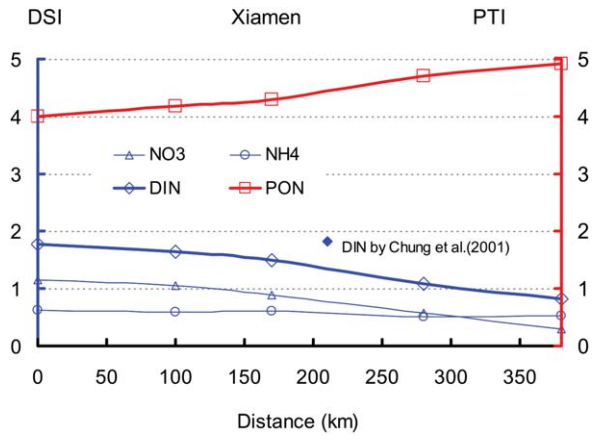

Figure 17. Fluxes (kmol s^{-1}) of various nitrigoneous components from the southern to the northern TWS.

approximately 1.8 and 4.0 kmol s^{-1}, respectively. The DIN decreases approximately 50% in the northern strait, particularly at the region between 150 and 300 km. The reason is that the strong onshore current at the bottom off Xiamen-PTI coast brings the nutrient upward. Consequently, the DIN and PON flux from the TWS into the ECS is roughly 0.8 and 5.0 kmol s^{-1}, respectively. The 90% reduction in DIN is attributed to NO_3 while the quick mineralization of organic matter maintains the stable concentration of NH_4 in the TWS (about 0.6 to 0.7 kmol s^{-1}).

[57] Understanding the nutrient fate is primary to the study of substance exchange between SCS and ECS, the estimated flux provides a reference to the regional environmental and fishery researches.

6. Summary

[58] The transport and fate of nutrients in the TWS in summer is studied by use of a physical-biological coupled circulation model. The model confirms that the NO_3 in the strait can be primarily traced to the upwelling subsurface water of the northern SCS. This upwelled NO_3 intrudes into the strait via two routes, i.e., western and eastern routes, separated by the TWB.

[59] The diagnostic analysis illustrates the advection and diffusion processes supply the NO_3 under and in the nitricline, respectively. The maximal depletion of NO_3 assembles around the nitrciline determined by the NO_3 transportation and light condition together. Moreover, the NO_3 is almost completely exhausted in the western route due to the shallow topography and the coastal upwelling, whereas this route contributes about 45% of the PON in the TWS, of which 30% can be attributed to the Pearl River. On the other hand, NO_3 transportation is conservative below the nitricline at the eastern route, which contributes the NO_3 supply in the TWS.

[60] The model estimates that the inputs of DIN and PON from the northern SCS are 1.8 and 4 kmol s^{-1}, respectively. Over half of the DIN is absorbed and transformed into PON in the strait. Consequently, the DIN and PON flux from the TWS to the ECS is estimated to be 0.8 and 5 kmol s^{-1}, respectively.

[61] This study is based on the climatological simulation of the ecosystem in the TWS, and the characters and mechanisms of nutrient fate, especially how the nutrient transport through the two routes, in the TWS during normal summer are described to some extents here. The higher reproducing capacity of the model and the abnormal variations of nutrient processes in the TWS need further interannual simulation and study in future.

Appendix A

Table A1. Abbreviations[1]

Abbreviation	Definition
DIN	Dissolved inorganic nitrogen
DNC	Degree of nutrient consumption
DSI	Dongshan Island
DSU	Dongshan upwelling
ECS	East China Sea
PHC	Penghu Channel
PHI	Penghu Islands
PON	Particulate organic nitrogen
PTI	Pingtan Island
PTU	Pingtan upwelling
SCM	Subsurface chlorophyll maximum
SCS	South China Sea
TN	Total nitrogen
TWB	Taiwan Bank
TWBU	Taiwan Bank upwelling
TWS	Taiwan Strait
WQD	Wuqiu Depression
ZYR	Zhangyun Rise

Appendix B: Skill Indices in Model Verification

[62] [1]Mean bias is defined as:

$$\mathrm{Mb} = \overline{p} - \overline{o} \tag{B1}$$

[63] Correlation coefficient as follows:

$$\mathrm{R} = \frac{\sum_{i=1}^{n}(o_i - \overline{o})(p_i - \overline{p})}{\sqrt{\sum_{i=1}^{n}(o_i - \overline{o})^2 \ \sum_{i=1}^{n}(p_i - \overline{p})^2}} \tag{B2}$$

[64] Root-mean-square is defined as:

$$\mathrm{RMS} = \sqrt{\frac{1}{n}\sum_{i=1}^{n}(p_i - o_i)^2} \tag{B3}$$

[65] Reliability index as follows:

$$\mathrm{RI} = e^{\varsigma}; \varsigma = \sqrt{\frac{1}{n}\sum_{i=1}^{n}\left(\log_{10}^{\left(\frac{p_i}{o_i}\right)}\right)^2} \tag{B4}$$

[66] Standard deviation (σ) is defined as:

$$\sigma_p = \sqrt{\frac{1}{n}\sum_{i=1}^{n}(p_i - \overline{p})^2} \tag{B5}$$

[67] Centered RMS difference as follows:

$$E' = \sqrt{\frac{1}{n}\sum_{i=1}^{n}[(p_i - \overline{p}) - (o_i - \overline{o})]^2} \tag{B6}$$

where p is the model result, o is the observed data, and n is the number of matching pairs. RI quantifies the average factor by which model predictions differ from observation. The ideal value of RI should be close to one when the model and observation are coincident. In case the data is log transformed in calculation the RMS, the exponential RMS is RI. The model and MODIS data are spatially interpolated onto the measurement positions before calculating these skill indices. In the verification, the observed data less than 0.1 μg L^{-1} for chlorophyll and 0.05 μM for NO_3 are excluded from the assessment.

[68] **Acknowledgments.** This work was supported by 973 Program (2009CB421200, 2013CB955700) from the National Basic Research Program of China and National Major Scientific Research Program of China, respectively; grants (41076001) from the Natural Science Foundation of China, grant (2010121029) from the Fundamental Research Funds for the Central Universities, and grant (2010Y0064) from the Science Foundation of Fujian Province. We would like to thank Kon-Kee Liu and three anonymous reviewers for their constructive suggestions to this manuscript.

References

Allen, S. E., and X. Durrieu de Madron (2009), A review of the role of submarine canyons in deep-ocean exchange with the shelf, *Ocean Sci. Discuss.*, *6*, 1369–1406.

Arthur, R. S. (1965), On the calculation of vertical motion in eastern boundary currents from determinations of horizontal motion, *J. Geophys. Res.*, *70*(12), 2799–2803.

Chau, K. W. (2005), An unsteady three-dimensional eutrophication model in Tolo Harbour, Hong Kong, *Mar. Pollut. Bull.*, *51*(8–12), 1078–1084.

Chen, C., D. A. Wiesenburg, and L. Xie (1997), Influences of river discharge on biological production in the inner shelf: A coupled biological and physical model of the Louisiana-Texas Shelf, *J. Mar. Res.*, *55*, 293–320.

Chen, C. T. A. (2008), Distributions of nutrients in the East China Sea and the South China Sea connection, *J. Oceanogr.*, *64*, 737–751.

Chen, C. T. A., L. Y. Hsing, C. L. Liu, and S. L. Wang (2004), Degree of nutrient consumption of upwelled water in the Taiwan Strait based on dissolved organic phosphorus or nitrogen, *Mar. Chem.*, *87*, 73–86.

Chung, S. W., S. Jan, and K. K. Liu (2001), Nutrient fluxes through Taiwan Strait in spring and summer 1999, *J. Oceanogr.*, *57*, 47–53.

Da Silva, A. M., C. C. Young, and S. Levitus (1994), Algorithms and procedures, in *Atlas of Surface Marine Data*, vol. *1*, NOAA Atlas NESDIS 6, p. 74, U.S. Gov. Printing Office, Washington, D. C.

Dinniman, M. S., M. K. John, and O. S. Walker (2003), Cross-shelf exchange in a model of the Ross Sea circulation and biogeochemistry, *Deep Sea. Res., Part II*, *50*, 3103–3120.

Druon, J. N., A. Mannino, S. Signorini, C. McClain, J. Wilkin, and K. Fennel (2010), Modeling the dynamics and export of dissolved organic matter in the Northeastern U.S. Continental shelf, *Estuarine Coastal Shelf Sci.*, *88*, 488–507.

Egbert, G., and S. Erofeeva (2002), Efficient inverse modeling of barotropic ocean tides, *J. Atmos. Oceanic Technol.*, *19*, 183–204.

Eppley, R. W. (1972), Temperature and phytoplankton growth in the sea, *Fish. Bull.*, *70*, 1063–1085.

Evans, G. T., and J. S. Parslow (1985), A model of annual plankton cycles, *Biol. Oceanogr.*, *3*, 327–347.

Fennel, K., J. Wilkin, J. Levin, J. Moisan, J. O'Reilly, and D. Haidvogel (2006), Nitrogen cycling in the Middle Atlantic Bight: Results from a three-dimensional model and implications for the North Atlantic nitrogen budget, *Global Biogeochem. Cycles*, *20*, GB3007, doi:10.1029/2005GB002456.

Gan, J., A. Cheung, X. Guo, and L. Li (2009), Intensified upwelling over a widened shelf in the northeastern South China Sea, *J. Geophys. Res.*, *114*, C09019, doi:10.1029/2007JC004660.

Gan, J., Z. Lu, M. Dai, A. Y. Y. Cheung, H. Liu, and P. Harrison (2010), Biological response to intensified upwelling and to a river plume in the northeastern South China Sea: A modeling study, *J. Geophys. Res.*, *115*, C09001, doi:10.1029/2009JC005569.

Hong, H. S., S. Y. Qiu, W. Q. Ruan, and Q. C. Hong (1991), Minnan-Taiwan Bank fishing ground upwelling ecosystem study, in *Minnan-Taiwan Bank Fishing Ground Upwelling Ecosystem Study (in Chinese)*, edited by H. S. Hong et al., pp. 1–18, Science, Beijing.

Hong, H. S., C. Y. Zhang, S. L. Shang, B. Q. Huang, Y. H. Li, X. D. Li, and S. M. Zhang (2009a), Interannual variability of summer coastal upwelling in the Taiwan Strait, *Cont. Shelf Res.*, *29*, 479–484.

Hong, H. S., Q. A. Zheng, J. Y. Hu, Z. Z. Chen, C. Y. Li, Y. W. Jiang, and Z. W. Wan (2009b), Three-dimensional structure of a low salinity tongue in the southern Taiwan Strait observed in the summer of 2005, *Acta Oceanol. Sin.*, *28*(4), 1–7.

Hong, H. S., C. T. A. Chen, Y. W. Jiang, J. Y. Lou, Z. Z. Chen, and J. Zhu (2011), Source water of two-pronged northward flow in the southern Taiwan Strait in summer, *J. Oceanogr.*, *67*, 385–393.

Hu, J., H. Kawamura, H. Hong, M. Suetsugu, and M. Lin (2001). Hydrographic and satellite observations of summertime upwelling in the Taiwan Strait: A preliminary description, *Terr. Atmos. Oceanic Sci.*, *12*(2), 415–430.

Hu, J. Y., H. Kawamura, C. Y. Li, H. S. Hong, and Y. W. Jiang (2010), Review on current and seawater volume transport through the Taiwan Strait, *J. Oceanogr.*, *66*, 591–610.

Hu, J. Y., H. S. Hong, Y. Li, Y. W. Jiang, Z. Z. Chen, J. Zhu, Z. W. Wan, Z. Y. Sun, and H. X. Liang (2011), Variable temperature, salinity and water mass structures in the southwestern Taiwan Strait in summer, *Cont. Shelf Res.*, *31*, S13–S23.

Ianson, D., and S. E. Allen (2002), A two-dimensional nitrogen and carbon flux model in a coastal upwelling region, *Global Biogeochem. Cycles*, *16*(1), 1011, doi:10.1029/2001GB001451.

Jan, S., C-S. Chern, and J. Wang (1994), A numerical study on currents in the Taiwan Strait during summertime, *Mer*, *32*, 225–234.

Jan, S., Y. H. Tseng, and D. E. Dietrich (2010), Sources of water in the Taiwan Strait. *J. Oceanogr.*, *66*, 211–221.

Jiang, Y. W., F. Chai, Z. W. Wan, X. Zhang, and H. S. Hong (2011), Characteristics and mechanisms of the upwelling in the southern Taiwan Strait: A three-dimensional numerical model study, *J. Oceanogr.*, *67*, 699–708, doi.10.1007/s10872-011-0080-x.

Lewis, M. R., J. J. Cullen, and T. Platt (1983), Phytoplankton and thermal structure in the upper ocean: Consequences of nonuniformity in chlorophyll profile, *J. Geophys. Res.*, *88*, 2565–2570.

Liu, G. M., and F. Chai (2009), Seasonal and interannual variability of primary and export production in the South China Sea: A three-dimensional physical–biogeochemical model study, *ICES J. Mar. Sci.*, *62*(2), 420–431.

Liu, K. K., S. Y. Chao, P. T. Shaw, G. C. Gong, C. C. Chen, and T. Y. Tang (2002), Monsoon-forced chlorophyll distribution and primary production in the South China Sea: Observations and a numerical study, *Deep Sea Res., Part I*, *49*, 1387–1412.

Liu, K. K., S. Y. Chao, H. J. Lee, G. C. Gong, and Y. C. Teng (2010), Seasonal variation of primary productivity in the East China Sea: A numerical study based on coupled physical-biogeochemical model, *Deep Sea Res., Part II*, *57*, 1762–1782.

Liu, S. M., G. H. Hong, J. Zhang, X. W. Ye, and X. L. Jiang (2009), Nutrient budgets for large Chinese estuaries, *Biogeosciences*, *6*, 2245–2263.

Lu, Z., J. Gan, M. Dai, and A. Y. Y. Cheung (2010), The influence of coastal upwelling and a river plume on the subsurface chlorophyll maximum over the shelf of the northeastern South China Sea, *J. Mar. Syst.*, *82*, 35–46.

Macías, D., P. J. S. Franks, M. D. Ohman, and M. R. Landry (2012), Modeling the effects of coastal wind- and wind–stress curl-driven upwellings on plankton dynamics in the Southern California current system, *J. Mar. Syst.*, *94*, 107–119.

Morel, A., and J.-F. Berthon (1989), Surface pigments, algal biomass profiles, and potential production of the euphotic layer: Relationships reinvestigated in view of remote-sensing applications, *Limnol. Oceanogr.*, *34*, 1545–1562.

Muttil, N., and K. W. Chau (2006), Neural network and genetic programming for modelling coastal algal blooms, *Int. J. Environ. Pollut.*, *28*(3–4), 223–238.

Naik, H., and C. T. A. Chen (2008), Biogeochemical cycling in the Taiwan Strait, *Estuarine Coastal Shelf Sci.*, *78*, 603–612.

Neumann, T. (2000), Towards a 3D-ecosystem model of the Baltic Sea, *J. Mar. Syst.*, *25*, 405–419.

Niemela, S., P. Paisanen, and H. Savijarvi (2001), Comparison of surface radiative flux parameterizations, Part II, Shortwave radiation, *Atmos. Res.*, *58*(2), 141–154.

Shang, S. L., H. S. Hong, C. Y. Zhang, S. P. Shang, and F. Chai (2004), Short-term variability of chlorophyll associated with upwelling events in the Taiwan Strait during the southwest monsoon of 1998, *Deep Sea Res., Part II*, *51*, 1113–1127.

Shchepetkin, A. F., and J. C. McWilliams (2005), The regional oceanic modeling system (ROMS): A split-explicit, free-surface, topography-following-coordinate oceanic model, *Ocean Modell.*, *9*, 347–404.

Soetaert, K., J. J. Middelburg, P. M. J. Herman, and K. Buis (2000), On the coupling of benthic and pelagic biogeochemical models, *Earth Sci. Rev.*, *51*, 173–201.

Song, Y. H., and D. Haidvogel (1994), A semi-implicit ocean circulation model using a generalized topography-following coordinate system, *J. Comput. Phys.*, *115*(1), 228–244.

Stow, C. A., J. Jolliff, D. J. McGillicuddy Jr., S. C. Doney, J. Allen, M. A.M. Friedrichs, K. A. Rose, and P. Wallhead (2009), Skill assessment for coupled biological/physical models of marine ststems, *J. Mar. Syst.*, *76*, 4–15.

Tang, D. L., D. R. Kester, I. H. Ni, H. Kawamura, and H.S. Hong (2002), Upwelling in the Taiwan Strait during the summer monsoon detected by satellite and shipboard measurements, *Remote Sens. Environ.*, *83*, 457–471.

Tang, D. L., H. Kawamura, and L. Guan (2004), Long-time observation of annual variation of Taiwan Strait upwelling in summer season, *Adv. Space Res.*, *33*, 307–312.

Taylor, K. E. (2001), Summarizing multiple aspects of model performance in a single diagram, *J. Geophys. Res.*, *106*(D7), 7183–7192.

Wu, J., S. W. Chung, L. S. Wen, K. K. Liu, Y. L. Chen, H. Y. Chen, and D. M. Karl (2003), Dissolved inorganic phosphorus, dissolved iron, and Trichodesmium in the oligotrophic South China Sea, *Global Biogeochem. Cycles*, *17*(1), 1008, doi:10.1029/2002GB001924.

Xu, J., Y. Wang, J. Yin, Q. Wang, F. Zhang, L. He, and C. Sun (2005), Transformation of dissolved inorganic nitrogen species and nitrification and denitrification processes in the near-sea section of Zhujiang river (in Chinese), *Acta Sci. Circum.*, *25*, 686–692.

Zhang, C., C. Hu, S. Shang, F. E. Müller-Karger, Y. Li, M. Dai, B. Huang, X. Ning, and H. Hong (2006), Bridging between SeaWiFS and MODIS for continuity of chlorophyll-a concentration assessments off Southeastern China, *Remote Sens. Environ.*, *102*, 250–263.